Tunable isolated attosecond X-ray pulses with gigawatt peak power from a free-electron laser

Joseph Duris [1,12], Siqi Li[1,2,12], Taran Driver [1,3,4], Elio G. Champenois[3], James P. MacArthur[1,2], Alberto A. Lutman[1], Zhen Zhang [1], Philipp Rosenberger[1,3,5,6], Jeff W. Aldrich[1], Ryan Coffee[1], Giacomo Coslovich[1], Franz-Josef Decker[1], James M. Glownia[1], Gregor Hartmann[7], Wolfram Helml [6,8,9], Andrei Kamalov[2,3], Jonas Knurr[3], Jacek Krzywinski[1], Ming-Fu Lin[1], Jon P. Marangos [4], Megan Nantel[1,2], Adi Natan [3], Jordan T. O'Neal[2,3], Niranjan Shivaram [1], Peter Walter[1], Anna Li Wang[3,10], James J. Welch[1], Thomas J. A. Wolf[3], Joseph Z. Xu[11], Matthias F. Kling [1,3,5,6], Philip H. Bucksbaum[1,2,3,10], Alexander Zholents[11], Zhirong Huang[1,10], James P. Cryan [1,3]* and Agostino Marinelli [1]*

[1]SLAC National Accelerator Laboratory, Menlo Park, CA, USA. [2]Physics Department, Stanford University, Stanford, CA, USA. [3]Stanford PULSE Institute, SLAC National Accelerator Laboratory, Menlo Park, CA, USA. [4]The Blackett Laboratory, Imperial College London, London, UK. [5]Max Planck Institute of Quantum Optics, Garching, Germany. [6]Physics Department, Ludwig-Maximilians-Universität Munich, Garching, Germany. [7]Institut für Physik und CINSaT, Universität Kassel, Kassel, Germany. [8]Zentrum für Synchrotronstrahlung, Technische Universität Dortmund, Dortmund, Germany. [9]Physik-Department E11, Technische Universität München, Garching, Germany. [10]Applied Physics Department, Stanford University, Stanford, CA, USA. [11]Argonne National Laboratory, Lemont, IL, USA. [12]These authors contributed equally: Joseph Duris, Siqi Li. *e-mail: jcryan@slac.stanford.edu; marinelli@slac.stanford.edu

Supplementary Information for Tunable Isolated Attosecond X-ray Pulses with Gigawatt Peak Power from a Free-Electron Laser

Joseph Duris,[1,*] Siqi Li,[1,2,*] Taran Driver,[1,3,4] Elio G. Champenois,[3]
James P. MacArthur,[1,2] Alberto A. Lutman,[1] Zhen Zhang,[1] Philipp Rosenberger,[1,3,5,6]
Jeff W. Aldrich,[1] Ryan Coffee,[1] Giacomo Coslovich,[1] Franz-Josef Decker,[1]
James M. Glownia,[1] Gregor Hartmann,[7] Wolfram Helml,[6,8,9] Andrei Kamalov,[2,3]
Jonas Knurr,[3] Jacek Krzywinski,[1] Ming-Fu Lin,[1] Jon P. Marangos,[4] Megan Nantel,[1,2]
Adi Natan,[3] Jordan T. O'Neal,[3,2] Niranjan Shivaram,[1] Peter Walter,[1] Anna Li Wang,[3,10]
James J. Welch,[1] Thomas J. A. Wolf,[3] Joseph Z. Xu,[11]
Matthias F. Kling,[1,3,5,6] Philip H. Bucksbaum,[1,3,2,10] Alexander Zholents,[11]
Zhirong Huang,[1,10] James P. Cryan,[1,3,†] and Agostino Marinelli[1,†]

[1]SLAC National Accelerator Laboratory, Menlo Park, CA, 94025, USA

[2]Physics Department, Stanford University, Stanford, CA, 94305, USA

[3]Stanford PULSE Institute, SLAC National Accelerator Laboratory, Menlo Park, CA, 94025, USA

[4]The Blackett Laboratory, Imperial College London, London, SW7 2AZ, UK

[5]Max Planck Institute of Quantum Optics, D-85748 Garching, Germany

[6]Physics Department, Ludwig-Maximilians-Universität Munich, 85748 Garching, Germany

[7]Institut für Physik und CINSaT, Universität Kassel, Heinrich-Plett-Str. 40, 34132 Kassel, Germany

[8]Zentrum für Synchrotronstrahlung, Technische Universität Dortmund,
Maria-Goeppert-Mayer-Straße 2, 44227 Dortmund, Germany

[9]Physik-Department E11, Technische Universität München,
James Franck-Straße 1, 85748 Garching, Germany

[10]Applied Physics Department, Stanford University, Stanford, CA, 94305, USA

[11]Argonne National Laboratory, Lemont, IL, 60439, USA

[*]These authors contributed equally to this work.

[†] To whom correspondence should be addressed: jcryan@slac.stanford.edu

[‡] To whom correspondence should be addressed: marinelli@slac.stanford.edu

1

Contents

1 Beam Dynamics and FEL Configuration

The accelerator and beamline parameters for the XLEAP experiment are described in the Methods section. The XLEAP beamline was designed to provide a modulation wavelength in the range between 2 and 4 μm for a beam energy between 3 and 5 GeV. At these beam energies the LCLS undulator produces photons with an energy between $\sim$400 and $\sim$1200 eV. The amplitude of the observed energy modulation is typically around a few MeV and can be fully compressed with the available dispersion of the XLEAP chicane. The self-modulation process has been described in detail in [44]. The radiation wavelength generated by the XFEL is given by the well known resonance formula [35]:

$$\lambda_r = \lambda_u \frac{1 + \frac{K_u^2}{2}}{2\gamma^2} \tag{1}$$

2

where γ is the Lorentz factor of the electron beam (between 6000 and 10000 for this experiment), λ_u and K_u are the undulator period and strength parameter, and λ_r is the radiation wavelength. Similarly, the radiation wavelength generated in the wiggler λ_{IR} (and therefore the electron beam modulation wavelength) is given by

$$\lambda_{IR} = \lambda_w \frac{1 + \frac{K_w^2}{2}}{2\gamma^2}. \tag{2}$$

The high-current spike created by the XLEAP modulator generates strong longitudinal space-charge forces which result in a strong time-energy correlation on the electrons within the spike [53]. The longitudinal space-charge force for a highly relativistic beam in an undulator with strength K is proportional to the derivative of the longitudinal current profile:

$$E_z(s) = -\frac{Z_0 I'(s)(1 + \frac{K^2}{2})}{4\pi\gamma^2} \left(2\log\left(\frac{\gamma\sigma_z}{r_b\sqrt{1 + \frac{K^2}{2}}} \right) \right) \tag{3}$$

where $I(s)$ is the beam current as a function of the longitudinal coordinate s, σ_z is the length of the current spike, and r_b is the beam radius. For a Gaussian-like spike such as the one generated by an ESASE modulator, the correlated energy spread (or chirp) is predominantly linear but has a non-vanishing non-linear component. The observed final energy distribution has a full width in the range between 30 and 40 MeV, over a spike duration of order 1 fs. The bandwidth of this chirp is much larger than the acceptance of the FEL.

To preserve the FEL gain with such a large energy spread, the undulator parameter K has to be varied (tapered) along the undulator length so that the resonant condition is maintained as the photons slip ahead of the electrons and interact with electrons of a different energy [53],[59, 60]. This chirp-taper matching condition can be expressed as:

$$\frac{K}{2 + K^2} \frac{dK_u}{dz} \lambda_u = \frac{\lambda_r}{\gamma} \frac{d\gamma}{ds}, \tag{4}$$

where z is the position along the undulator beamline. The chirp-taper matching condition can only be verified for a specific value of the linear chirp $d\gamma/ds$, meaning that if we optimise

the undulator to lase in the ESASE spike, the rest of the bunch will be mismatched in energy, therefore suppressing the background radiation outside of the main pulse. Furthermore it can be shown that the cubic chirp introduced by space-charge contributes to shortening the pulse duration when the taper is optimised to compensate the linear chirp [60].

To take advantage of these two effects, we maximised the chirp introduced by space-charge by only allowing the electron beam to lase in the last few sections of our undulator beamline, and suppressing the FEL gain in the first part of the undulator by introducing a large transverse oscillation in the electron beam trajectory. Figure S1 shows an example of a typical undulator configuration for an ESASE experiment. The last 7 undulators are used for lasing, while the remaining 24 are used to maximise the energy chirp introduced by space-charge. The electron beam trajectory is also plotted, showing a large vertical oscillation in the first 24 undulators to suppress the FEL gain.

The space-charge induced energy-spread can be seen in Fig. 1-e of the main text, which shows the measured time-energy distribution of the full electron bunch. The ESASE current spike is seen as a large vertical stripe, i.e. a short region of the bunch with a large energy spread. The resolution of our diagnostic is not enough to resolve the sub-fs structure of the phase space, and therefore the chirp of the ESASE spike itself appears as a vertical stripe with no apparent time-energy correlation.

The delay chicane used in the double bunch experiment is a four-dipole magnetic chicane. The chicane was originally built as part of the hard X-ray self-seeding experiment and relevant technical information can be found in [61]. The dipoles are powered by a DC power supply and the current is controlled with 16 bit precision. The delay is proportional to the current squared and can be varied from 0 to 50 fs. Further control of the delay can be achieved with trim coils that allow for sub-X-ray wavelength control. The delay can be changed in a matter of seconds and requires minimal reconfiguration of the beamline to cancel residual uncompensated kicks
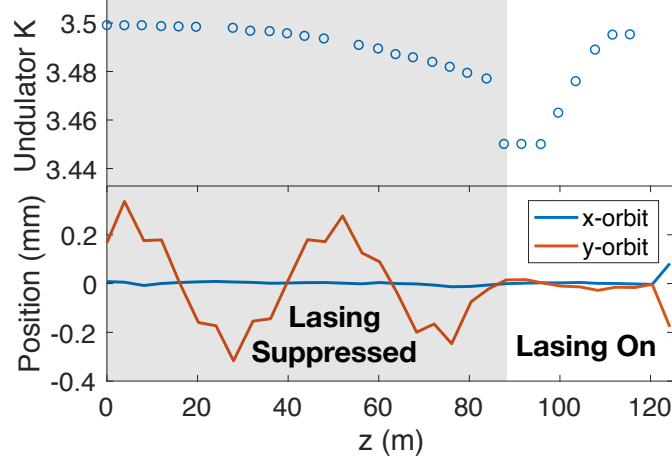
4

Figure S1: Top: typical undulator configuration for an ESASE experiment. The FEL gain is suppressed in the first 24 undulators by a large oscillation in the vertical trajectory of the electron beam. Bottom: measured vertical and horizontal trajectory through the undulators.

from the magnets.

2 Longitudinal Phase Space Measurements

The time-energy distribution of the electrons (the longitudinal phase space) can be measured on a shot-by-shot basis in a non-destructive fashion (i.e. without intercepting or otherwise affecting the X-rays). The measurements are performed with an X-band transverse cavity placed in the dump line of the LCLS [41].

Figures 1-c,d,e of the main article are a zoomed-in version of the full measured electron beam phase space. Figure S2 reports the entire longitudinal phase space measurement for the same shots. To better represent the phase space in the XLEAP beamline we have numerically removed the energy variation introduced by the wakefield of the undulator vacuum chamber from Figures 1-c,d,e. The X-band transverse cavity diagnostic does not have enough temporal
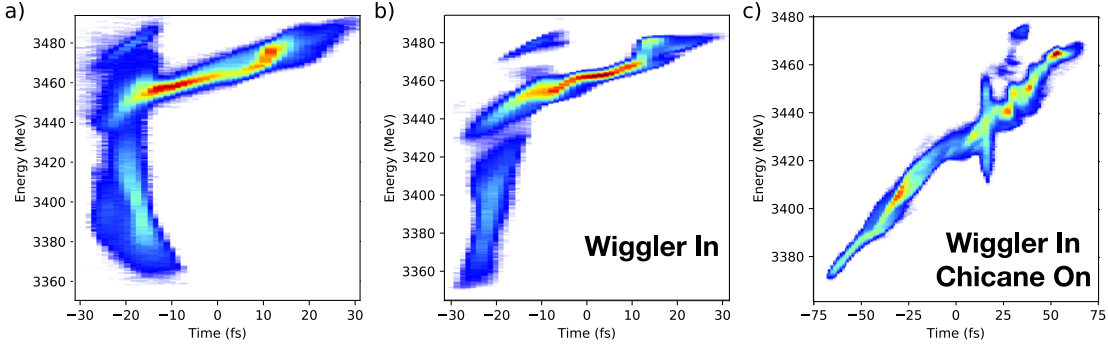
Figure S2: Measured longitudinal phase space for three configurations: (a) wiggler out and chicane off, (b) wiggler in and chicane off, (c) wiggler in and chicane on. The data in Figs. 1-b,c,d,e was processed from these three measurements.

resolution to measure the duration of the ESASE spike in Fig. 1-e, but numerical simulations of this technique suggest that the peak current is close to 10 kA, with a spike duration of roughly 1 fs.

The self-modulation process is inherently stable to current fluctuations in the electron beam because the phase and wavelength of the modulation are entirely dependent on the ponderomotive phase in the wiggler [62]. The measured modulation typically exhibits phase and wavelength jitter at the few-hundred attosecond level [62]. The amplitude jitter can be as low as 10%. The XTCAV does not have enough resolution to measure the peak current in the spike, however one can infer the relative shot-to-shot current fluctuation level from a measurement of the energy spread in the current spike. Figure S3 shows a scatter plot of the energy spread as a function of the peak current before the XLEAP modulator (measured at the second bunch compressor) for a fixed beam energy of 3.42 GeV. For a Gaussian spike current distribution, assuming that the energy spread is dominated by the space-charge contribution, the fluctuations in the spike peak current I_{spike} are related to the shot-to-shot jitter in the energy spread σ_E by:

$$\frac{\delta I_{\mathrm{spike}}}{I_{\mathrm{spike}}} \simeq \frac{1}{2} \frac{\delta \sigma_E}{\sigma_E} \qquad (5)$$
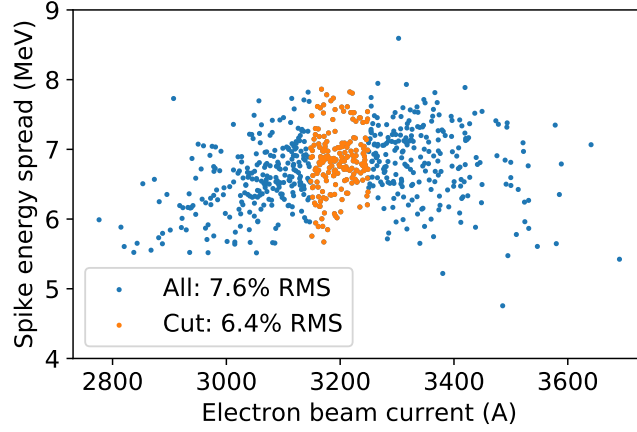
6

Figure S3: Single-shot measurement of the space-charge induced energy spread in the ESASE current spike (measured as the width of an energy window containing 50% of the charge in the spike) as a function of electron bunch peak current at the second bunch compressor.

This equation assumes that the charge in the spike is constant, which is a good assumption as long as the modulation wavelength and the initial current don't jitter significantly. In Fig. S3 the energy spread has an RMS jitter of 7.6% for the entire distribution and 6.4% if one selects a narrow distribution of initial peak current. This corresponds to a 3.8% RMS peak current jitter in the ESASE spike (reduced to 3.2% for a fixed BC2 peak current).

3   Angular Streaking Setup

Our experiment was performed at the Atomic, Molecular, and Optical physics (AMO) beamline of the Linac Coherent Light Source (LCLS). The streaking laser pulse is derived from a 120 Hz titanium-doped sapphire laser system synchronised to the accelerator. 10 mJ, 800 nm laser pulses are compressed to ~ 40 fs, and the compressed pulse is used to pump an optical parametric amplifier (TOPAS-HE, Light Conversion) which produces 500 µJ pulses at a wavelength of 1300 nm. The 1300 nm pulse is spectrally filtered to remove any residual pump light or any other colours made by the OPA. A quarter waveplate (Thorlabs AQWP05M-1600) is
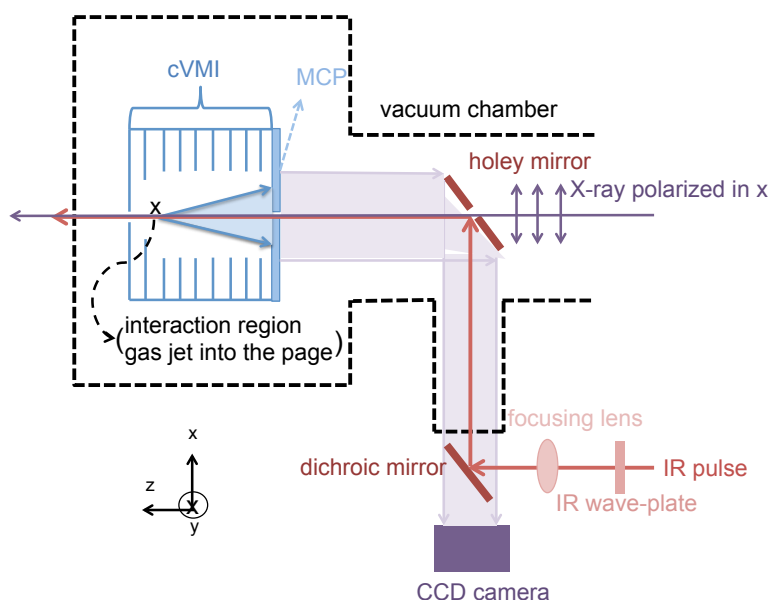
Figure S4: Experimental geometry of the co-axial velocity map imaging (c-VMI) apparatus used in the angular streaking setup. Linearly polarised X-rays pass through a 2 mm hole in a silver coated mirror before coming to a focus in the interaction region of the cVMI spectrometer. Photoelectrons are extracted by the electrostatic field of the spectrometer, in the direction opposite to the X-ray propagation. The phosphor screen of the charged particle detector is imaged via the holey silver mirror, through a dichroic mirror used to introduce an IR laser pulse. The polarisation of the IR pulse is controlled via a quarter wave-plate upstream of the dichroic mirror. The target gas is introduced via a skimmed molecular beam oriented in the y-direction.

used to produce circularly polarised laser pulses, which are then focussed with a $f = 750$ mm CaF$_2$ lens. As shown in Fig. S4, a dichroic mirror (R1300/T400-550) is used to steer the beam into a vacuum chamber. The streaking laser field is combined with the FEL beam using a silver mirror with a 2 mm drilled hole, and both pulses come to a common focus in the interaction region of a co-axial velocity map imaging (c-VMI) apparatus [45]. To generate a reference measurement, the streaking laser was intentionally mistimed every 11 XFEL shots. The c-VMI used here is designed for angular streaking applications, and the device is described in Ref. [45]. The X-ray focal spot size is approximately ∼55μm diameter (FWHM), while the streaking laser focus has a substantially larger ∼110 μm diameter. A target gas is introduced via a molecular beam source. For the two X-ray photon energies considered in the main text, we use neon as the target for 905 eV pulses and CO_2 as the target for 570 eV pulses.

Photoelectrons produced by two-colour ionisation are extracted opposite to the laser propagation direction, as shown in Fig. S4. This geometry is used to minimise any signal from scattered X-ray photons. Extracted electrons are detected with a microchannel plate detector coupled to a P43 phosphor screen (Photonis). The phosphor screen is imaged onto a high-speed CCD camera (Opal1k) via the 2 mm holey mirror which couples the streaking laser into the chamber, and through the dichroic mirror. The CCD camera records images of the phosphor screen at the repetition rate of the accelerator: 120 Hz.

We can diagnose the streaking laser polarisation using the photoelectron momentum distribution from strong-field ionisation of a carbon dioxide (CO_2) target. Figure S5 shows the two-dimensional projection of the photoelectron momentum distribution produced by ionisation with the 1300 nm laser. We can estimate the ellipticity of the streaking laser by comparing the ionisation probability along the major and minor axes of the laser polarisation. Using ADK theory, the differential ionisation rate shown in Figure S5 gives a rough estimate of $\epsilon \gtrsim 0.95$ for the ellipticity of the IR streaking laser.
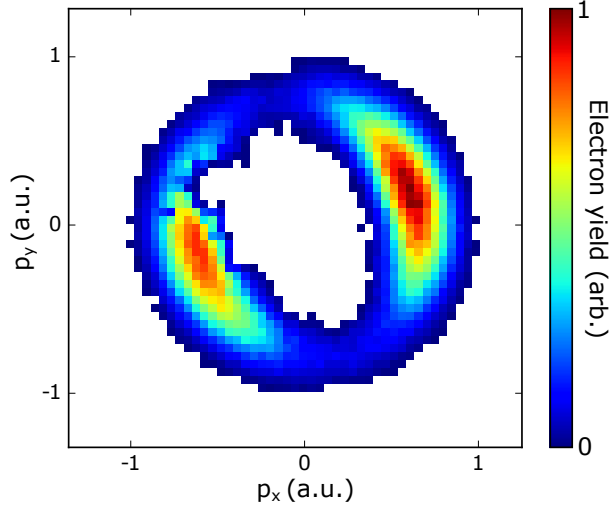
9

Figure S5: Two-dimensional projection of the photoelectron momentum distribution generated by the IR laser in CO_2 gas jet. This data was integrated over 4×10^4 laser shots. The ratio of ionisation along the major axis to the minor axis is 10:1, which corresponds to an ellipticity of $\epsilon \gtrsim 0.95$.

3.1 Laser X-ray Timing Stability

Synchronisation between the attosecond X-ray pulses and the streaking pulses is a persistent challenge in our measurement. Measurements at the LCLS use conventional feedback techniques to stabilise the optical laser pulse arrival time relative to a radio frequency (RF) reference from the accelerator [51]. The primary sources for the temporal jitter include thermal effects, RF noise, and energy jitter in the electron bunch. The electron bunches accumulate additional temporal jitter as they propagate along the acceleration and bunch compression chain. This energy jitter is directly transformed into a timing jitter in the magnetic chicane bunch compressors. Using a transverse cavity just before the electron beam dump, we can measure the shot-to-shot variation between the arrival time of the electron bunch and the RF reference. Figure S6 shows the distribution of measured streaking magnitudes for each shot as a function of the bunch arrival time (BAT). The peak of the streaking magnitude distribution is offset from the nominal 0 fs BAT by ~60 fs due to a slight mistiming of the streaking laser. We observe streaking over
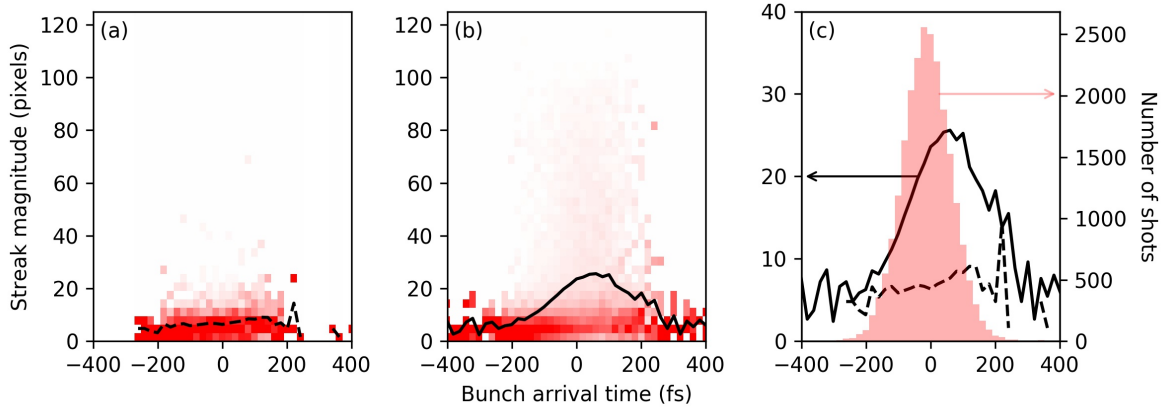
10

Figure S6: Distributions of the extracted streak magnitudes as a function of the bunch arrival time with (a) a mistimed streaking laser and (b) a co-timed streaking laser. The black curves show the average streaking magnitude. (c) Comparison of the streaking magnitude's dependence on the bunch arrival time (black, left axis) and the distribution of bunch arrival times (red, right axis).

a ∼300 fs range of BATs. This range is affected by both the streaking laser pulse width and the streaking laser timing jitter with respect to the RF reference.

4 Photoelectron Data Analysis Procedure

We select shots to analyse based on the single shot pulse energy, streaking angle, and streaking amplitude. Pulse energy is measured in the standard non-intrusive method employed at the LCLS, by recording the fluorescence induced by the X-ray pulse in a small (0.02–1.2 Torr) pressure of nitrogen [63]. Filtering on pulse energy ensures the analysed shots have a high number of electron counts, which provides better quality reconstructions. A number of complementary techniques provide real-time information on the shot-to-shot amplitude and direction of the momentum shift from the streaking laser. To process the shots, we identify these two streaking coordinates using a genetic optimisation algorithm which approximates the centroid of the shifted electron distribution, by maximising the electron density falling in an open ring
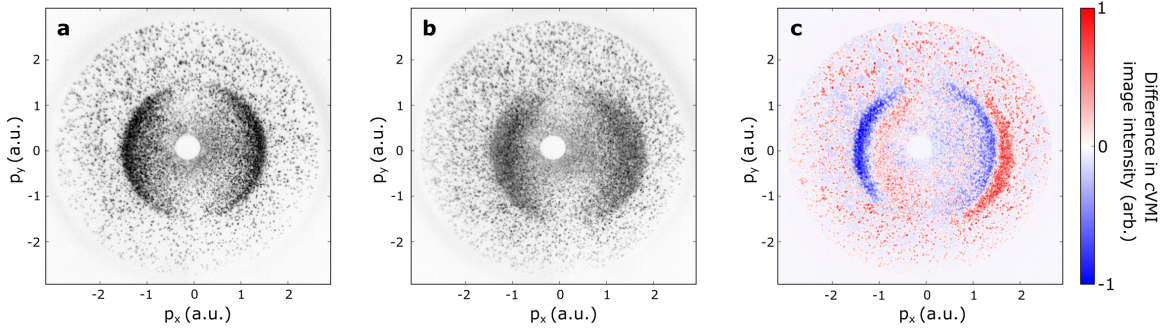
11

Figure S7: Measurement of photoelectrons by the c-VMI. (a) Raw, unprocessed image of a single-shot measurement of neon 1s photoelectrons ionised by a 905 eV ESASE pulse without the streaking laser. (b) Raw single-shot image of neon 1s photoelectrons measured at the same photon energy in the presence of the circularly polarised streaking field, shifting the momentum distribution of the photoelectrons and encoding the properties of the ESASE pulse. This shift is made clear in panel (c), showing the difference in measured electron yield between the shot shown in panel (b) and a background image constructed from multiple measurements of the unstreaked photoelectron distribution.

shape as the shape is shifted across the c-VMI image [64]. For the reconstruction, we select shots that are streaked perpendicular to the X-ray polarisation, within an angular acceptance of $\sim 40°/\sim 65°$ for the 905 eV and 570 eV shots respectively. This is a result of the 6 mm hole in the center of the detector [45] and the angular distribution of the photoelectrons produced by the two-colour ionisation, which approaches a $\cos^2\theta$ dipole distribution (see Fig. S7). Shots streaked parallel to the X-ray polarisation suffer from a greater distortion of signal because the corresponding momentum shift is along the axis of the highest electron density, maximising the electron signal lost by virtue of 'falling' into the hole. The converse is true for shots streaked perpendicular to the X-ray polarisation. We have verified that the measured pulse duration is not correlated with either pulse energy or streak angle.

Single-shot CCD images, representative examples of which are shown in Fig. S7, are analysed in the following way. First, a quadrant dependent gain correction is applied to the image to account for the variation in camera gain between the four quadrants of the detector, and we

shift the center of the image to match the symmetry centre found from unstreaked images. Then we apply a median filter with a neighbourhood size of 19 pixels, and the resulting image is convolved with a Gaussian filter ($\sigma = 25$ pixels). The filtered image is then downsized from the initial 1024×1024 image to 32×32 pixels. A background image, primarily consisting of low energy electrons at the center of the detector, was obtained from the unstreaked images. This background is subtracted from the downsized image. Subtraction of this background from a single shot image inevitably leads to small negative values in some pixels. Following background subtraction, we threshold the image by setting to zero all pixels with absolute value smaller than the absolute value of the most negative pixel in the background-subtracted image. Incomplete suppression of the electron background for the 905 eV pulse measurements results in a small artefact in the time domain pulse reconstruction (a $< 10\%$ feature appearing exactly half the streaking laser period away from the measured pulse). This is removed in post-processing.

5 Reconstruction Algorithm

The pulse reconstruction algorithm is described in our previous publication [49].The algorithm is based on the forward propagation of a basis set. We assume that the photoionised electron wavepacket (EWP) can be described by a set of basis functions, α_n:

$$\psi(t) = \vec{E}_X(t) \cdot \vec{d}(\vec{p} - \vec{A}(t)) = \sum_n c_n \, \alpha_n(t). \tag{6}$$

The EWP, $\psi(t)$, is given by the product of the X-ray electric field, $\vec{E}_X(t)$, and the dipole moment, $\vec{d}(\vec{p})$, describing the X-ray photoionisation process, and $\vec{A}(t)$ is the vector potential of the streaking laser field. The two-colour photoelectron momentum distribution for an arbitrary X-ray pulse can be calculated in the strong field approximation (SFA) [65]:

$$b(\vec{p}) \;\; = \;\; \int_{-\infty}^{\infty} \vec{E}_X(t) \cdot \vec{d}(\vec{p} - \vec{A}(t)) \, e^{-i\Phi(t)} \, dt, \tag{7}$$

13

$$\Phi(t) = \int_t^\infty dt' \left\{ \frac{(\vec{p} - \vec{A}(t'))^2}{2} + I_p \right\}, \tag{8}$$

$b(\vec{p})$ is the probability amplitude for observing an electron with momentum $\vec{p}$, and I_p is the binding energy of the ionised electron. We assume the dipole moment is described by a hydrogenic model: $\vec{d}(\vec{p}) = \vec{p}/(|\vec{p}|^2 - 2I_p)^3$. Each basis function, $\alpha_n(t)$, will produce a probability amplitude, $a_n(\vec{p})$, for observing an electron with momentum $\vec{p}$ according to

$$a_n(\vec{p}) = \int_{-\infty}^\infty \vec{\alpha}_n(t) \cdot \vec{d}(\vec{p} - \vec{A}(t)) \, e^{-i\Phi(t)} \, dt. \tag{9}$$

The total probability amplitude, $b(\vec{p})$, for the EWP in Eq. 6 is given by

$$b(\vec{p}) = \sum_n c_n a_n(\vec{p}). \tag{10}$$

The measured photoelectron momentum distribution is given by

$$B(\vec{P}) = \int dp_z \, |b(\vec{p})|^2 = \sum_{nm} c_m^* c_n \int dp_z a_m^*(\vec{p}) a_n(\vec{p}), \tag{11}$$

where $\vec{P}$ is the two-dimensional vector describing the projected momentum. While Eqs. 7–14 are general for any choice of basis function, in this work we choose to construct the basis functions α_n by forward-propagating a set of X-ray pulses described by the von Neumann functions, which are a joint time-frequency basis:

$$\alpha_{ij}(t) = \left(\frac{1}{2\alpha\pi} \right)^{1/4} \exp\left[-\frac{1}{4\alpha}(t - t_j)^2 - it\omega_i \right]. \tag{12}$$

where α is a constant specified by the von Neumann lattice range and size, and the lattice points (t_i, w_j) are distributed on a 6×6 grid [66]. The total time window for the von Neumann lattice is chosen to be one period of the streaking laser field (4.3 fs for a central frequency of 1.3 µm). The number of lattice points is selected empirically to produce a reliable reconstruction, which captures the requisite structure of sub-femtosecond pulses and at the same time does not suffer from high frequency artefacts introduced by fitting too many basis functions for the
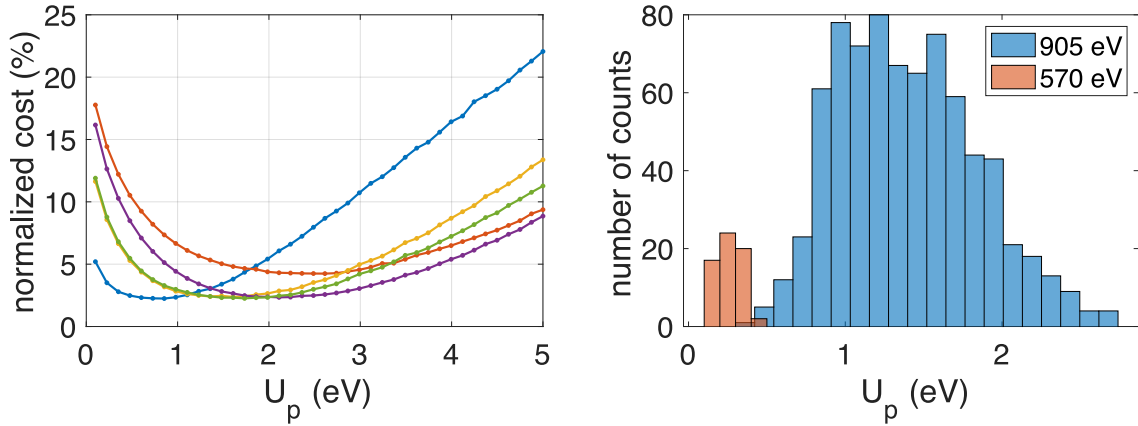
Figure S8: Left: Examples of U_p scan for five different shots. Normalized cost is defined as L_G in Eq. 14 divided by the sum of image intensity squared. Right: distribution of U_p for the analysed shots.

small image size. A 6×6 von Neumann lattice corresponds to 36 points in the time domain representation, giving a temporal spacing of 120 as for the temporal reconstruction.

We use a non-linear minimisation routine to fit the measured single-shot electron distribution to the basis set constructed from each von Neumann function. The likelihood estimator L measures the agreement between the simulated data from Eq. 11 and the actual data, D:

$$L_G = \sum_i \left| D_i - B(\vec{P}_i) \right|^2, \tag{13}$$

$$L_P = \sum_i \left\{ B(\vec{P}_i) - D_i \ln[B(\vec{P}_i)] + \ln[D_i!] \right\}, \tag{14}$$

where i indexes the pixels of the measurement. L_G is the maximum likelihood estimator in the case of Gaussian distributed noise, whereas L_P is the maximum likelihood estimator in the case of Poisson distributed noise. Both likelihood estimators were tested and provide similar results. Use of the von Neumann representation affords a sparse representation of the X-ray pulse, which assists in the robustness of the non-linear fitting routine.

As described above, the relative phase between the X-ray pulse and the streaking pulse is random, and we do not have knowledge of the instantaneous value of the vector potential
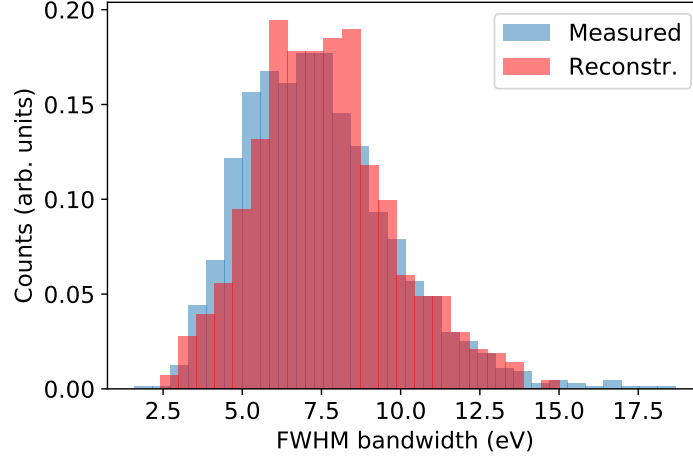
15

Figure S9: Bandwidth distributions from spectrometer measurements at 905 eV (blue) and reconstructed shots from streaking measurements at 905 eV.

amplitude, or the ponderomotive potential, U_p, responsible for the momentum shift. As shown in [49], we find the optimal U_p for each shot by scanning the likelihood estimator, Eq. 14, as a function of U_p with a range from 0.5 to 5 eV. The likelihood estimator varies smoothly with U_p, showing a clear minimum which identifies the optimal U_p (see Fig. S8).

The basis images (Eq. 11) are calculated on a 64×64 grid and downsized to 32×32 to prevent numerical artefacts, and then convolved with a Gaussian filter with a kernel size chosen to match the convolution strength of the Gaussian filter applied to the experimental data (i.e. kernel width $\sigma = 25$ pixels on a 1024×1024 grid).

The non-linear fitting search is initiated by random numbers for the coefficients based on Monte Carlo sampling. For each shot, we run 20 iterations of the reconstruction algorithm with different initial values and check the convergence by comparing each solution. The time domain profile of the X-ray field is given by,

$$E_X(t) = \sum_n c_n \alpha_n(t), \tag{15}$$

where c_n are the optimal coefficients returned by the algorithm. We then take the Fourier trans-
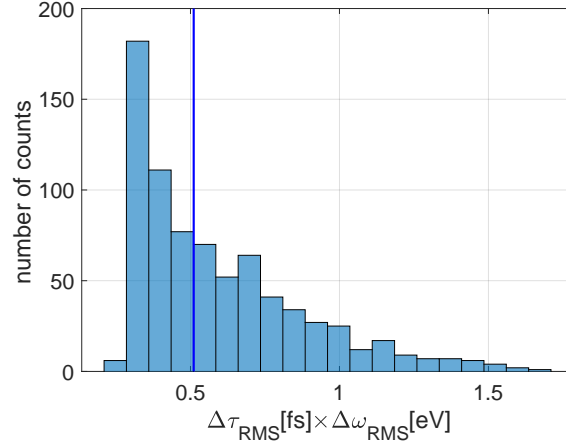
16

Figure S10: Distribution of time-frequency RMS bandwidth product of 905 eV data. The vertical blue line indicates the median of the distribution at 0.51.

form of the time-domain X-ray field profile to obtain the spectral domain profile.

Note that the spectral domain is sensitive to spiky structures in the time domain profile which are artefacts of the algorithm due to Poisson noise. To mitigate this problem, we apply a Gaussian filter to the time domain field profile with a width of $\sigma_t = 170$ as for 570 eV and $\sigma_t = 120$ as for 905 eV. The Gaussian filter width is comparable to the basis function lattice grid size (120 as). With this Gaussian filter, the statistical distribution of the FWHM bandwidth obtained from the reconstruction closely matches the spectrometer data (see Fig. S9), which provides an independent benchmark for the reconstruction method.

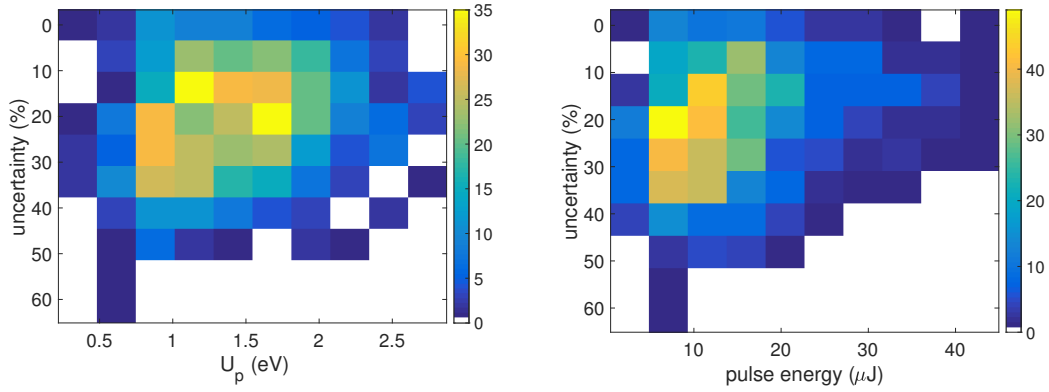Figure S10 shows the distribution of time-frequency bandwidth products measured from the

Figure S11: Distribution of pulse duration uncertainty as a function of streaking amplitude (left) and pulse energy (right).

reconstructed pulses. For a Fourier-transform limited Gaussian pulse, the time-frequency RMS bandwidth product should be 0.32 and the average time-bandwidth product is within a factor two of this value.

We note that a direct measurement of the frequency chirp in the X-ray pulses was not possible due to lack of resolution in the phase reconstruction. The X-ray chirp can be inferred from the undulator taper required for optimal FEL performance, using Eq. 4 and converting the electron beam chirp into the corresponding X-ray chirp using the FEL resonance equation:

$$\frac{1}{E_{photon}}\frac{dE_{photon}}{dt} \simeq 2\frac{1}{\gamma}\frac{d\gamma}{dt}. \tag{16}$$

The resulting chirp is roughly 12 eV/fs (5 eV/fs) for the 920 eV (605 eV) data sets. We note that a 12 eV/fs chirp on a 280 as pulse would result in a total bandwidth of 7.25 eV, consistent with the median bandwidth from spectrometer data (7.5 eV). This amount of chirp is also consistent with the time-bandwidth product measured from the streaked pulse reconstruction.

5.1 Quantification of Single-Shot Experimental Uncertainty

The reconstruction algorithm can converge to different solutions for a given pulse due to the finite number of counts in each shot and the finite resolution of the VMI. These different solu-

tions all match the measured data with good accuracy, with an average integrated residual of 3%. As described below, the different solutions all give very similar temporal profiles. We employ the statistical distribution of these independent reconstructions to identify the most probable solution as well as the experimental uncertainty of the pulse profile and pulse duration.

To determine the most probable solution, we calculate the inner product between each of the 20 solutions (i.e. $< I_i, I_j > / \sqrt{< I_i, I_i >< I_j, I_j >}$ with $i, j = $ 1,2,...,20) for each shot in the time domain. We then identify the most probable solution as the one with the highest average inner product between itself and all other reconstructions, which is the solution shown as the red curve in Fig. 2 of the main text. For a given shot, the standard deviation of the inner product of each solution with the averaged (most probable) pulse profile is a measure of the uncertainty on the overall pulse profile, and it has a value of 7 % (10%).

To obtain an estimate of the pulse duration uncertainty we calculate the standard deviation of the pulse duration found by the 20 solutions. We define the uncertainty to be $\sigma (\Delta\tau_{\mathrm{RMS}})/\Delta\tau_{\mathrm{RMS}}$, where σ is the standard deviation. The median of the uncertainty distribution is 20% (28%) for 905 eV (570 eV). Figure S11 shows that the pulse duration uncertainty correlates with the streaking amplitude and the pulse energy, indicating that the uncertainty is smaller for higher streaking amplitude as well as for higher pulse energy. The dependence on the streaking amplitude comes from the decreasing angular resolution corresponding to a small radius on the detector. In the limiting case where the streaking amplitude is zero, there is complete degeneracy across the time axis. The dependence on higher pulse energy can be explained by a stronger signal to noise ratio as more X-rays create more photoelectrons in the gas jet.

We also performed independent reconstructions on simulated data for different Poisson sampling. We found that the statistical distribution of the pulse properties for different reconstructions of a given Poisson sample are similar to the statistics over different Poisson samples. This confirms that the uncertainty over independent reconstructions is consistent with the experimen-
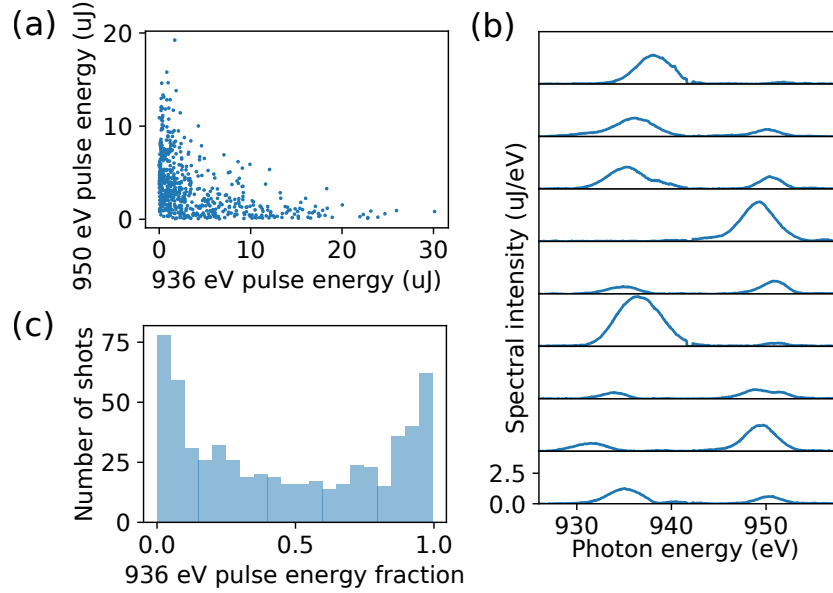
Figure S12: Single-shot spectral measurements for the two-colour experiment. (a) Single-shot measurement of the intensity of each pulse. (b) Representative single-shot spectra for the two-colour setup. (c) Histogram of the fraction of the total pulse energy in each pulse.

tal uncertainty, as discussed above.

6   Two-Colour Pulse Properties

The characteristic intensity jitter of single-spike sub-fs FELs is also observed in the double-pulse operation. Figure S12 (a) shows a scatter plot of the pulse energy contained in the two pulses from shot-to-shot. The pulse energy in each pulse has close to 100% fluctuations, and the intensities of the two pulses are anti-correlated, a well known property of the split undulator method [55]. This is because when running the system as close as possible to saturation, a large increase in the energy of the first pulse spoils the energy-spread of the electron beam, causing the second pulse to be weaker. One could improve the relative pulse stability at the cost of a reduced peak power by interrupting the gain of the first pulse earlier and reducing the effect of the first pulse on the second.

20

Figure S12 (b) shows a few examples of single shot two-colour spectra, while Fig. S12 (c) is a histogram of the relative intensities of the two pulses. Whilst the source has significant intensity jitter, the pulse energy is so large that the properties can be measured on a single-shot basis for all the shots with non-destructive diagnostics. Therefore one could apply this method to time-resolved pump/probe experiments and sort the data based on single-shot measurements of the pulse properties.

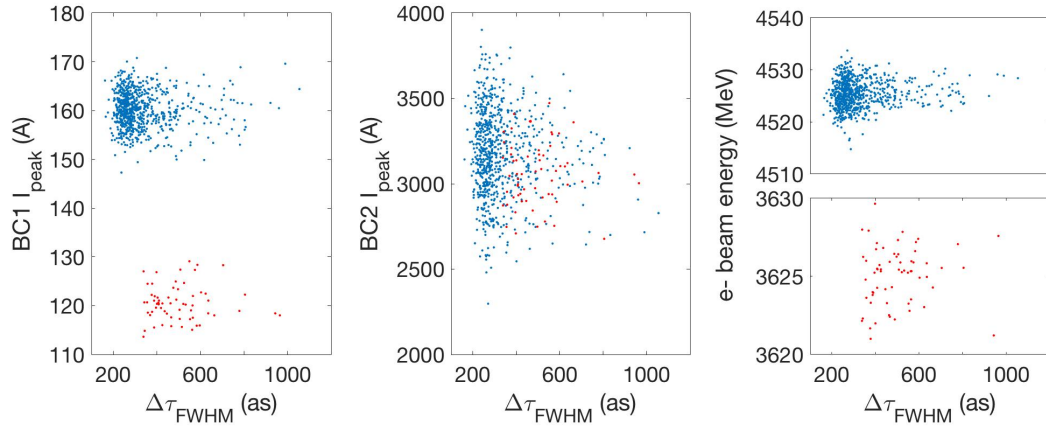# 7 Machine Parameter Correlations

Figure S13: Scatter plots of machine parameters and the retrieved pulse durations. The blue dots are for the neon data at 905 eV, and the red dots are for the CO_2 data at 570 eV.

We have examined the correlation between the retrieved pulse duration and a number of critical machine parameters: the peak electron beam current measured at bunch compressors 1 and 2 (BC1 and BC2) and the electron beam energy after acceleration. Figure S13 shows that there is no clear correlation between either of these parameters and the measured pulse duration (the calculated correlation coefficients are all below 0.2).

We have also investigated the dependence of photon energy on the electron beam energy and peak electron beam current. In standard operation, the electron beam energy measured af-
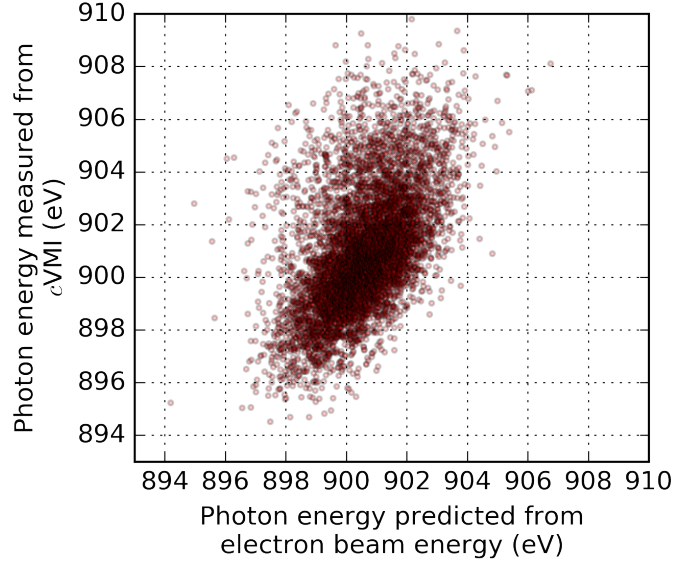
Figure S14: Scatter plot of shot-to-shot central photon energy as predicted by the electron beam energy (x-axis) and measured using the cVMI (y-axis).

ter acceleration provides a reliable shot-to-shot indicator of the central photon energy, which naturally jitters due to the stochastic nature of SASE. We tested whether the beam energy remained a good predictor of single-shot central photon energy in ESASE operation. To do so, we take 7371 shots at 905 eV operation with the streaking laser intentionally mistimed, and directly measure the central photon energy of each shot from the neon 1s photoelectrons collected by the cVMI. For each shot we then compare this value with the expected central photon energy according to measured the electron beam energy. This can be calculated using the well-known quadratic dependence of photon energy on electron beam energy described by the FEL resonance condition (Eq. 1). Figure S14 shows a shot-to-shot scatter plot of the predicted photon energy from the electron beam energy and the measured photon energy from the cVMI. Unlike for standard SASE operation, the electron beam energy does not accurately predict the central photon energy. The RMS deviation between predicted and measured photon energy is 2.0 eV, and the FWHM of the distribution of deviations for this dataset is 3.5 eV. This value of the
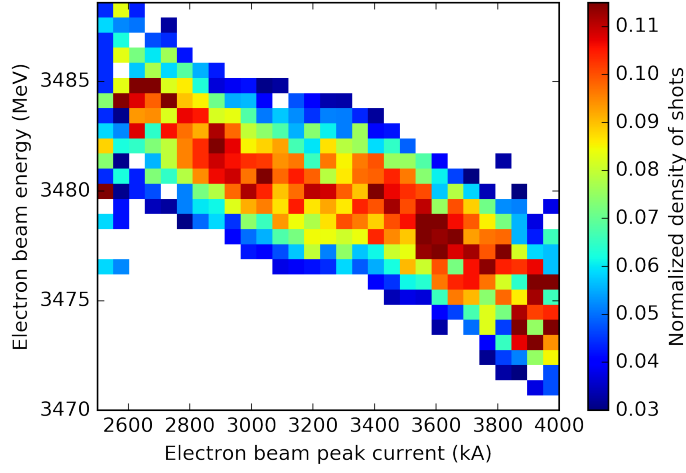
Figure S15: Measured values of electron beam energy and peak current for photon energy fixed to a small (< 0.4 eV) window around ~ 546 eV. The histogram counts have been normalised to have the same integrated value in each peak current bin.

spread of deviations is configuration dependent and has been observed as 4.6 eV at different configurations. For this reason, the use of a single-shot photon energy diagnostic, which could simply be an electron spectrometer, is very useful for measurements performed using ESASE. We note that the electron beam energy predicts the average central photon energy of a collection of shots with comparable accuracy to SASE operation.

In ESASE operation, the central photon energy is also dependent on the peak electron beam current, which we measure at bunch compressors 1 and 2 (BC1 and BC2). This dependence can be seen in Fig. S15. For this figure, we select 18,079 shots where the streaking laser has been intentionally mistimed and which have a central photon energy, measured using the cVMI, fixed to a small window of ± 0.2 eV around ~ 546 eV. We plot the electron beam energy measured after acceleration and the peak current measured at BC2, for each of these shots. This shows that the central photon energy depends on both quantities. A larger electron beam energy can be compensated by a smaller peak current to produce the same photon energy, and vice-versa.

23

References

[59] Saldin, E. L., Schneidmiller, E. A. & Yurkov, M. V. Self-amplified spontaneous emission fel with energy-chirped electron beam and its application for generation of attosecond x-ray pulses. *Phys. Rev. ST Accel. Beams* **9**, 050702 (2006). URL `http://link.aps.org/doi/10.1103/PhysRevSTAB.9.050702`.

[60] Baxevanis, P., Duris, J., Huang, Z. & Marinelli, A. Time-domain analysis of attosecond pulse generation in an x-ray free-electron laser. *Phys. Rev. Accel. Beams* **21**, 110702 (2018). URL `https://link.aps.org/doi/10.1103/PhysRevAccelBeams.21.110702`.

[61] Amann, J. *et al.* Demonstration of self-seeding in a hard-x-ray free-electron laser. *Nature photonics* **6**, 693 (2012).

[62] MacArthur, J., Duris, J., Huang, Z., Marinelli, A. & Zhang, Z. Self-Modulation of a Relativistic Electron Beam in a Wiggler. In *Proc. 9th International Particle Accelerator Conference (IPAC'18), Vancouver, BC, Canada, April 29-May 4, 2018*, no. 9 in International Particle Accelerator Conference, 4492–4495 (JACoW Publishing, Geneva, Switzerland, 2018). URL `http://jacow.org/ipac2018/papers/thpmk083.pdf`. Https://doi.org/10.18429/JACoW-IPAC2018-THPMK083.

[63] Moeller, S. *et al.* Photon beamlines and diagnostics at LCLS. *Nuclear Instruments and Methods in Physics Research Section A: Accelerators, Spectrometers, Detectors and Associated Equipment* **635**, S6–S11 (2011). URL `http://www.sciencedirect.com/science/article/pii/S0168900210024101`.

[64] Storn, R. & Price, K. Differential Evolution A Simple and Efficient Heuristic for global Optimization over Continuous Spaces. *Journal of Global Optimization* **11**, 341–359 (1997). URL https://doi.org/10.1023/A:1008202821328.

[65] Kitzler, M., Milosevic, N., Scrinzi, A., Krausz, F. & Brabec, T. Quantum Theory of Attosecond XUV Pulse Measurement by Laser Dressed Photoionization. *Physical Review Letters* **88**, 173904 (2002). URL https://link.aps.org/doi/10.1103/PhysRevLett.88.173904.

[66] Fechner, S., Dimler, F., Brixner, T., Gerber, G. & Tannor, D. J. The von Neumann picture: a new representation for ultrashort laser pulses. *Optics Express* **15**, 15387–15401 (2007). URL https://www.osapublishing.org/abstract.cfm?uri=oe-15-23-15387.